Contents lists available at ScienceDirect

Ore Geology Reviews

journal homepage: www.elsevier.com/locate/oregeorev

Fluorescent sphalerite rich in tungsten, copper, gallium, silver, and other elements from the Cordilleran-style, polymetallic veins of Philipsburg, Montana

Celine M.E. Beaucamp [a,*], Christopher H. Gammons [a], Jay M. Thompson [b], Heather A. Lowers [b]

[a] Montana Technological University, Butte, MT, USA
[b] U.S. Geological Survey, Denver, CO, USA

ARTICLE INFO

Keywords:
Porphyry-lode deposit
Coupled substitution
Photoluminescence
LA-ICP-MS
Raman spectroscopy

ABSTRACT

Sphalerite from the central, high-sulfidation zone (enargite-stable) of the Philipsburg polymetallic mining district, southwest Montana, displays unusually bright fluorescence (red, orange, yellow, blue, purple, green) under longwave UV light (365 nm). LA-ICP-MS analysis reveals the fluorescent sphalerite has very low Fe (average < 100 ppm) and variable content of other trace elements that correlate to luminescence color banding. Mean/maximum content (in ppm) in fluorescent sphalerite for selected elements are 5.7/7900 Ag, 107/11800 As, 1400/4730 Cd, 917/30400 Cu, 381/5000 Ga, 32/696 Ge, 119/2130 In, 230/8190 Mn, 43/3000 Pb, 16/1700 Sb, and 89/1980 W. This study is the first to document elevated tungsten content (>10 ppm) in sphalerite. Copper is closely correlated with Ga, consistent with the coupled substitution: $Cu^{+} + Ga^{3+} = 2Zn^{2+}$. Similar coupled substitution reactions can be written for Ag^{+}, In^{3+}, As^{3+}, Sb^{3+}, Bi^{3+}, and Ge^{4+}. However, the brightest red fluorescent bands are most closely related to the unexpected presence of W. Sphalerite with high Cu and Ga but lacking W fluoresces yellow and shows a single Raman peak at 349 cm^{-1} corresponding to pure sphalerite. In contrast, red-fluorescent sphalerite shows the presence of a second peak at 427 cm^{-1} that increases in intensity with increased W content. We propose that tungsten enters the sphalerite lattice as W^{6+} via a substitution such as $W^{6+} + 4Cu^{+} = 5Zn^{2+}$ and that this substitution creates lattice strain that results in the anomalous fluorescence and Raman signals. Sphalerite bands with low concentrations of Cu and Ga fluoresce blue or green. Vivid blue fluorescence is displayed by sphalerite with high Cd (>1000 ppm) but low concentrations of all other trace elements. Sphalerite from the low-sulfidation peripheral mines of the Philipsburg district contains high Fe (>10,000 ppm) and does not fluoresce. Nonetheless, this sphalerite is also highly enriched in trace metals, including Ag (mean 2480/max 8660 ppm), Cu (1610/3440), Mn (7020/8100), and Sb (1960/6390). The results of this study underscore the importance of including tungsten in the list of analytes in future studies of trace elements in sphalerite. In addition, a hand-held UV lamp may be a rapid and cost-effective method to screen sphalerite of variable composition in outcrop or drill core. It may be a useful exploration tool to vector towards a high-sulfidation zone of a zoned porphyry or epithermal deposit, when it is present.

1. Introduction

Sphalerite is a common and essential mineral in the study of ore deposits. It may host a wide range of trace elements, including, but not limited to Ag, As, Bi, Cd, Co, Cu, Ga, Ge, Hg, In, Mn, Mo, Ni, Pb, Sb, Sn, Te, and Tl (Goldschmidt, 1930; Oftedal, 1941; Stoiber, 1940; Rose, 1967; Cook et al., 2009; Ye et al., 2011; Frenzel et al., 2016; Benites et al., 2021; Torró et al., 2023). Notably, the iron content of sphalerite in equilibrium with pyrite and/or pyrrhotite is an indicator of sulfur fugacity (fS_2) during mineral deposition (Barton and Toulmin, 1966). The advent of laser ablation inductively coupled plasma mass spectrometry (LA-ICP-MS) has dramatically accelerated our understanding of the range of concentrations of trace elements in sphalerite (Cook et al., 2009; Ye et al., 2011). Furthermore, many elements listed above are critical to the economy and defense of sovereign nations when the global supply chain is uncertain (Burton, 2022). Cadmium, Ga, Ge, and In are currently recovered as a byproduct of metallurgical processing of sphalerite-bearing ores (Frenzel et al., 2016).

* Corresponding author at: 1300 West Park Street, Dept. of Geological Engineering, Montana Technological University, Butte, MT 59701, USA.
E-mail address: cbeaucamp@mtech.edu (C.M.E. Beaucamp).

https://doi.org/10.1016/j.oregeorev.2024.106267
Received 27 June 2024; Received in revised form 26 September 2024; Accepted 28 September 2024

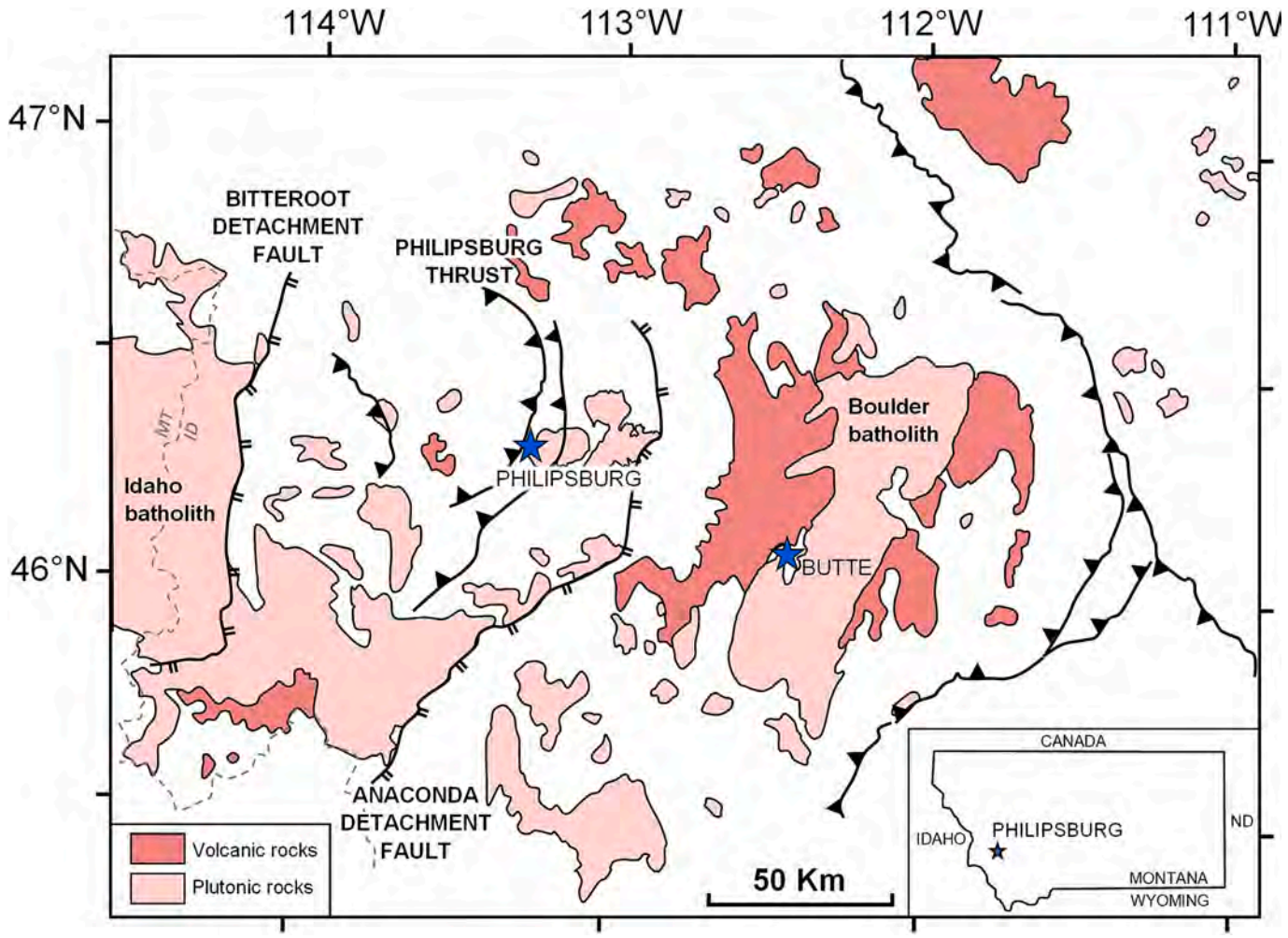

Fig. 1. Regional geologic context. The Philipsburg mining district sits between the western border of the Philipsburg batholith and the Philipsburg thrust. Modified from Foster et al. (2012). MT: Montana, ID: Idaho, ND: North Dakota.

Cordilleran polymetallic deposits, as described by Catchpole (2011) and Fontboté and Bendezú (2009), contain an extensive suite of base and precious metals hosted by quartz-carbonate-sulfide veins and mantos that are concentrically zoned around a deeper porphyry Cu-Mo system. At Butte, Montana, the type example of the Cordilleran-style lode deposits, the zonation can be simplified as Cu-Ag → Cu-Zn-Ag → Ag-Zn-Pb-Mn as the distance from the porphyry increases (Dilles, 2004). Ortelli (2015) performed LA-ICP-MS on sphalerite across the Butte District and found highly elevated Ag, Cd, Cu, Fe, Ga, In, Mn, and Sn concentrations. However, few clear zonation trends were found, and no effort was made to examine trace element inter-correlations. Other Cordilleran polymetallic deposits that have been investigated for trace element patterns in sphalerite include Morococha, Peru (Benites et al., 2021), Colquijirca, Peru (Ortiz-Benavente et al., 2022), Cerro de Pasco, Peru (Rottier et al., 2018), Ayawilca, Peru (Benites et al. 2022), and Bingham Canyon, USA (Tomlinson et al. 2021). Sphalerite samples from these deposits contain variable amounts of Ag, As, Cd, Cu, Fe, Ga, Ge, In, Mn, Pb, Sb, Sn, and W. Some previous workers (e.g., Oftedal, 1941; Cook et al., 2009; Frenzel et al., 2016; Benites et al., 2021) have noted trends in trace-element composition with respect to temperature and/or sulfur fugacity (e.g., high vs. intermediate vs. low sulfidation mineral assemblages), although such correlations tend to be limited to one deposit and have undocumented transferability to other districts.

The present paper expands on our knowledge of trace elements in sphalerite from Cordilleran polymetallic deposits by examining samples from the historic Philipsburg district, Montana. Philipsburg shares many similarities to its famous neighbor, Butte, which is located 68 km to the southeast. A unique aspect of sphalerite from Philipsburg is its vivid, multicolored fluorescence under long-wave UV light (Beaucamp et al., 2022). Like Butte, the veins of Philipsburg show chemical and mineralogical zonation away from a Cu-Mo porphyry (Beaucamp and Gammons, 2022). Most of these veins contain abundant sphalerite, making a study of district-wide zonation in trace element systematics possible.

1.1. Site description

The Philipsburg mining district was active between 1864 and the 1980's and produced over 24 M oz of Ag, 83,000 oz of Au, 36 M kg of Zn, 10 M kg of Pb, 1.8 M kg of Cu, and 295,000 metric tons of Mn (Prinz, 1967). Additionally, about 206 tons of WO_3 (mainly from scheelite) were produced from the nearby districts of Black Pine-Henderson (9 miles), Foster Creek (11 miles), and Silver Lake (14 miles). Scheelite, powellite, and huebnerite mineralization were recorded at several sites within the Philipsburg Mining District itself, although W production is not mentioned (Walker, 1960). These numbers make Philipsburg the second most productive polymetallic mining district in Montana, after the more famous deposits of Butte. Both districts are located in a portion of the Sevier fold-and-thrust belt of the Cordillera that has been intruded by large granitoid bodies of late Cretaceous age (Naibert et al., 2010; Fig. 1). Thrust faults in the area have dominantly west-dipping, N-S strikes (O'Connell, 2001; Naibert et al., 2010; Foster et al., 2012), and include the Philipsburg Thrust immediately west of the study area.

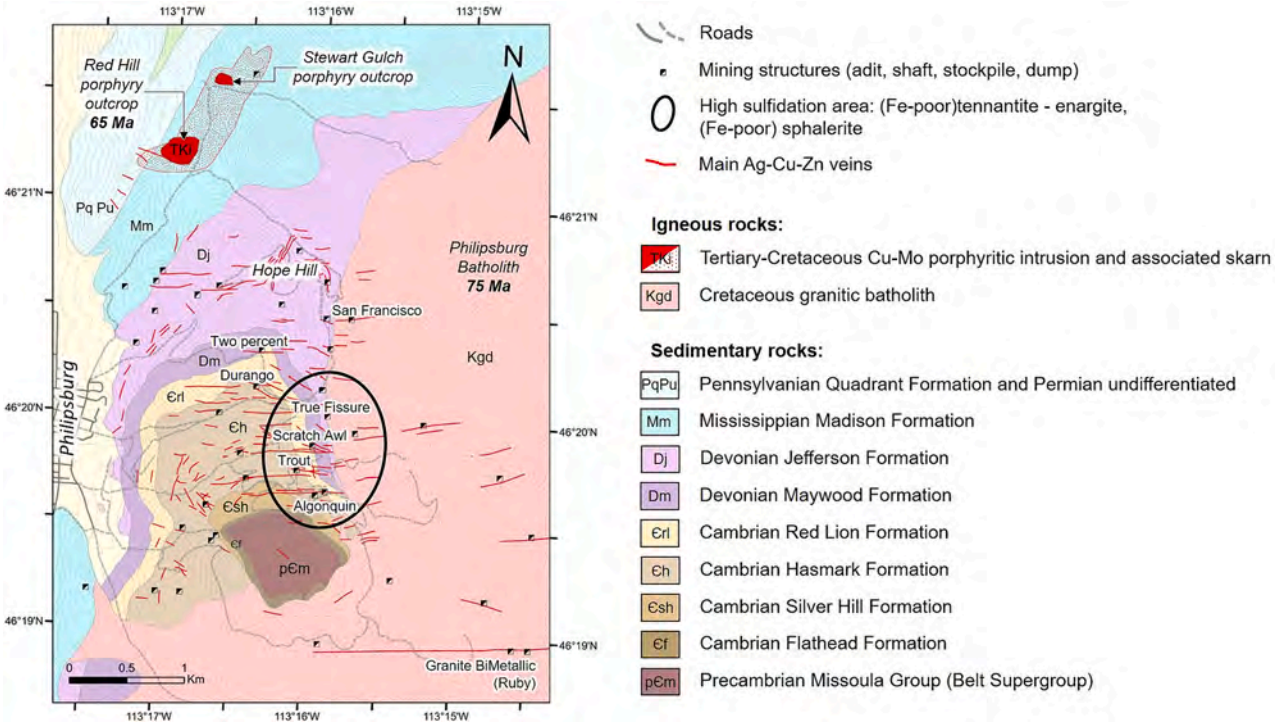

Fig. 2. Geology of the Philipsburg mining district (modified from Prinz, 1967). The circled area shows the approximate extent of the high sulfidation zone, which contains all the highly fluorescent sphalerite samples.

Extension of the orogenic belt began in the Paleogene with shallow detachment faults (e.g., the Bitterroot and Anaconda detachment faults, Fig. 1). The extension continued into the Neogene with steep normal faults (Foster et al., 2010).

A sequence of Mesoproterozoic through Cretaceous metasedimentary rocks intruded by late Cretaceous granitic plutons and porphyry stocks hosts the polymetallic veins of the Philipsburg District (Fig. 2). The oldest sedimentary units are quartzites of the Belt Supergroup and overlying Cambrian Flathead Formation. These are overlain by a thick sequence of Cambrian to Mississippian limestones and dolostones and, in turn, Pennsylvania and Permian quartzite, chert, and phosphatic black shale. The formations young to the north along the axis of an asymmetrical north-plunging anticline and are truncated to the south and east by the ~ 75 Ma Bimetallic Stock of the Philipsburg Batholith (Emmons and Calkins, 1913; Goddard, 1940; Naibert et al., 2010). Contact metamorphism occurs in a < 2 km-wide belt around the batholith (Holser, 1950; Hyndman et al., 1972). Two outcrops of hydrothermally altered porphyritic rock (Worthington, 2007) at the district's northern end have been drilled for porphyry-skarn Cu-Mo mineralization. The westernmost outcrop was dated at ~ 65 Ma (U-Pb on zircons, F. Dudas, personal communication). Nearby silver-bearing quartz veins on Hope Hill follow bedding planes in calcareous formations and yielded the first ores mined in the area (Prinz, 1967). South of Hope Hill, numerous E-W trending, steeply dipping, Ag-Zn-Pb-bearing quartz veins cut both the Cretaceous granite and the sedimentary rocks and were the most prolific veins of the district (Prinz, 1967). The mineral assemblages suggest a district zonation similar to other Cordilleran polymetallic lode deposits (central Mo-Cu > Ag-Cu > Ag-Zn-Cu > Ag-Pb-Zn-$MnCO_3$ ± Au in the peripheral zone). Veins rich in enargite and low-Fe sphalerite in the Scratch Awl, True Fissure, Trout, and Algonquin mines indicate the possible presence of a high-sulfidation center at depth (Beaucamp and Gammons, 2022). In contrast, mines to the south, including the Granite-Bimetallic mine (the largest producer in the district), have a low-sulfidation assemblage.

2. Methods

Samples examined in this study were obtained from mine dumps and small ore stockpiles in the Philipsburg district, with permission from the landowners. Any vein specimens that contained fresh sulfides were sampled. Over 100 samples were collected. From this collection, representative samples for each mine containing sphalerite were selected for further detailed study, regardless of the presence or absence of strong UV fluorescence. Each sample was split with a water-cooled tile saw and photographed in ambient and long-wave UV light. Ten samples were sent to a commercial lab for preparation of polished thick (60 μm) sections. Several dozen additional samples were mounted in epoxy 1-inch rounds and polished. All samples were examined using reflected and transmitted light microscopy. Selected samples were examined by X-ray diffraction (XRD) using an Olympus Terra instrument at the Department of Geological Engineering of Montana Technological University (MTU). Initial petrographic analysis was accomplished using a combination of reflected/transmitted light microscopy and scanning electron microscopy-energy dispersive X-ray spectrometry (SEM-EDS) at the CAMP lab of MTU. Backscatter electron (BSE) images were taken on a Tescan MIRA 3 GMU – TIMA X field emission scanning electron microscope (FESEM) and elemental analysis acquisition was accomplished with an EDAX Octane Elect energy dispersive X-ray spectrometer. Sphalerites from selected samples were analyzed by Raman spectroscopy employing a Renishaw spectrometer and 514 nm laser operated at 100 % power, with 30-second collection times. Raman spectra were collected from polished samples that were previously analyzed by LA-ICP-MS. By focusing the Raman laser beam immediately next to the LA-ICP-MS ablation pits, it was possible to make correlations between the Raman spectra and the trace element concentrations of different sphalerite growth bands. The XRD and Raman patterns showed no indication of wurtzite (hexagonal ZnS), which is consistent with the absence of anisotropic domains in the samples when viewed under reflected light.

Hyperspectral cathodoluminescence (HCL) was used to help target individual LA-ICP-MS points. HCL data were collected at the Denver

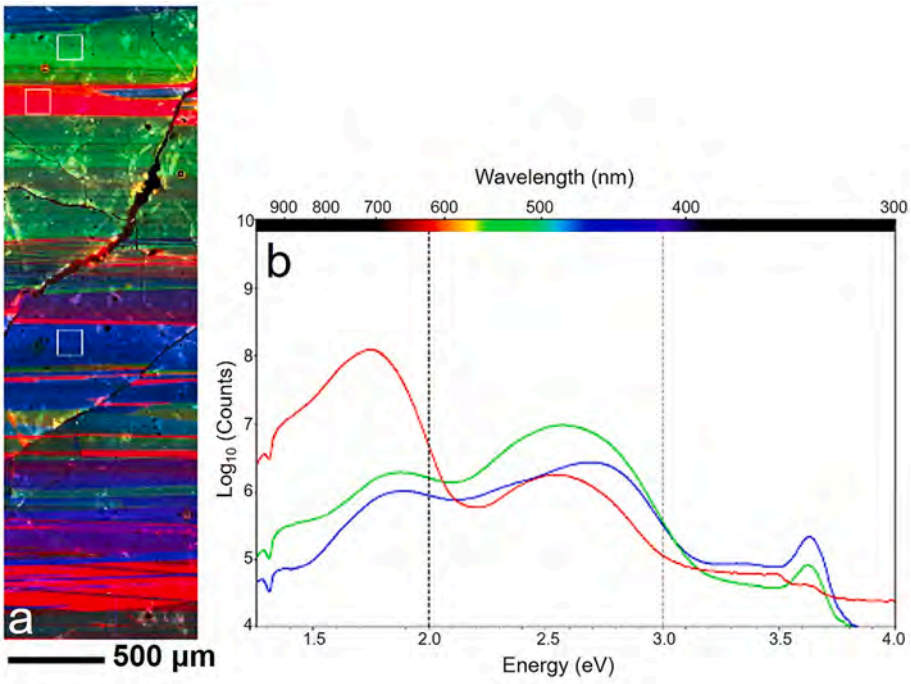

Fig. 3. Example hyperspectral cathodoluminescence (HCL) data. a) red (1.2–2 eV), green (2–3 eV), and blue (3–4 eV) composite overlay of a portion of sample CB-SA-22; b) sum spectrum from squares within red, green, and blue areas is shown for comparison. (For interpretation of the references to color in this figure legend, the reader is referred to the web version of this article.)

Microbeam Laboratory at the U.S. Geological Survey in Denver, Colorado, with an xCLent hardware and software system on a JEOL 8530F Plus electron microprobe operated at 20 kV accelerating voltage, 30nA (cup) beam current, 20 ms dwell, and 1–10 µm step size depending on the area to cover. The spectra were broken into three regions of interest, 1.3–2 eV, 2–3 eV, and 3–4 eV, and assigned to red, green, and blue channels, respectively, to generate false-color images (Fig. 3). These images were of superior resolution compared to photographs taken under UV light, and proved invaluable to guide the selection of points for LA-ICP-MS analysis. Further research is underway to deconvolute the HCL spectra and potentially assign elements to the peaks present.

Laser ablation ICP-MS analyses were performed at the USGS-LTRACE laboratory at the U.S. Geological Survey in Denver, Colorado. Analyses were performed using a Photon Machines Analyte G2 laser ablation system that houses an ATL-EX-SI ArF excimer laser source and operates at 193 nm wavelength and ~ 5 ns pulse width. The laser system was coupled to an Agilent 8900 quadrupole ICP-MS operated in single quadrupole mode. Ablations were performed in an atmosphere of pure (99.99 %) helium flowing at a 0.6 l/ min in the two-volume HelEx ablation cell. The aerosol and helium gas were immediately mixed with argon gas in a pushfit 'Y' connector using Nylon 6 tubing. Ablations were performed using a 30 µm square beam, 3.5 J/cm^2 laser fluence, and a 10 Hz laser repetition rate.

Forty-nine elements (51 isotopes) were measured: ^{7}Li, ^{23}Na, ^{24}Mg, ^{27}Al, ^{29}Si, ^{31}P, ^{34}S, ^{39}K, ^{44}Ca, ^{47}Ti, ^{51}V, ^{53}Cr, ^{55}Mn, ^{57}Fe, ^{59}Co, ^{60}Ni, ^{63}Cu, ^{66}Zn, ^{71}Ga, ^{73}Ge, ^{74}Ge, ^{75}As, ^{77}Se, ^{85}Rb, ^{88}Sr, ^{89}Y, ^{90}Zr, ^{93}Nb, ^{95}Mo, ^{109}Ag, ^{111}Cd, ^{115}In, ^{118}Sn, ^{121}Sb, ^{125}Te, ^{137}Ba, ^{139}La, ^{140}Ce, ^{172}Yb, ^{182}W, ^{185}Re, ^{195}Pt, ^{197}Au, ^{202}Hg, ^{205}Tl, ^{206}Pb, ^{207}Pb, ^{208}Pb, ^{209}Bi, ^{232}Th, and ^{238}U. Elements/isotope concentrations were calibrated using element-dependent combinations of NIST610, MASS-1, and GSE-1 g basaltic glass reference materials. Details on calibration are given in the electronic appendix 1. Data reduction was performed using the LADR software (version: 1.1.08_20230105) using ^{57}Fe as the internal standard element. For quantification, each cation typically found in sphalerite was stoichiometrically paired to one S^{-2} anion, and the sum of the cations plus calculated S (in a 1 to 1 ratio for most elements) were normalized to 100 % total. Lithophile elements (e.g., Si) were assumed to be present as small inclusions combined with oxygen in typical oxidation states and included in the 100 % total for the sphalerite. However, these inclusions generally constituted < 0.2 % of the analysis. Tennantite analyses were quantified similarly but with a different cation-to-S ratio. The basaltic reference glass BHVO-2 g was analyzed as an unknown for quality control, but with all cations as oxides (Fe as Fe^{2+}) and then normalized to 100 %. Sulfur is only measured to confirm the mineral phase and is not quantified.

Elemental mapping by LA-ICP-MS was also performed but using a 20 µm square beam rastered from left to right at 20 µm/sec, at a 10 Hz laser pulse rate, and then offset by 20 µm in the Y direction so that the total image area was 1500 µm x 3600 µm. A smaller element list compared to spot analyses was used for elemental mapping to give a shorter sweep time (0.3184 s vs. 0.559 s for spot analysis). Element maps were also produced using LADR software. Quantification was as previously described for spot analyses but was performed for each pixel (quadrupole readout) using the same quantification procedure as spot analyses, but with calibration materials run as line scans under the same ablation conditions.

Sphalerite samples for LA-ICP-MS analysis were selected based on their fluorescence intensity (or lack thereof) and location across the district. Twelve samples were analyzed from eight different mines. The filtered dataset from the spot analyses consists of 379 laser analyses: 312 points for fluorescent sphalerite and 49 for non-fluorescent sphalerite. Analyses with laser-ablation profiles showing evidence of solid inclusions were deleted, ensuring that the measured content of trace elements in the filtered dataset is present in solid solution in the ZnS lattice. For the element-correlation graphs, contents in ppm (mg/kg) were first converted to mmol/kg by dividing by the gram formula weights of each element (i). These values were then divided by the sum of the mmol/kg values for all elements in the solid and multiplied by 10^6 to get content values in "atomic content in ppm," or ppma.

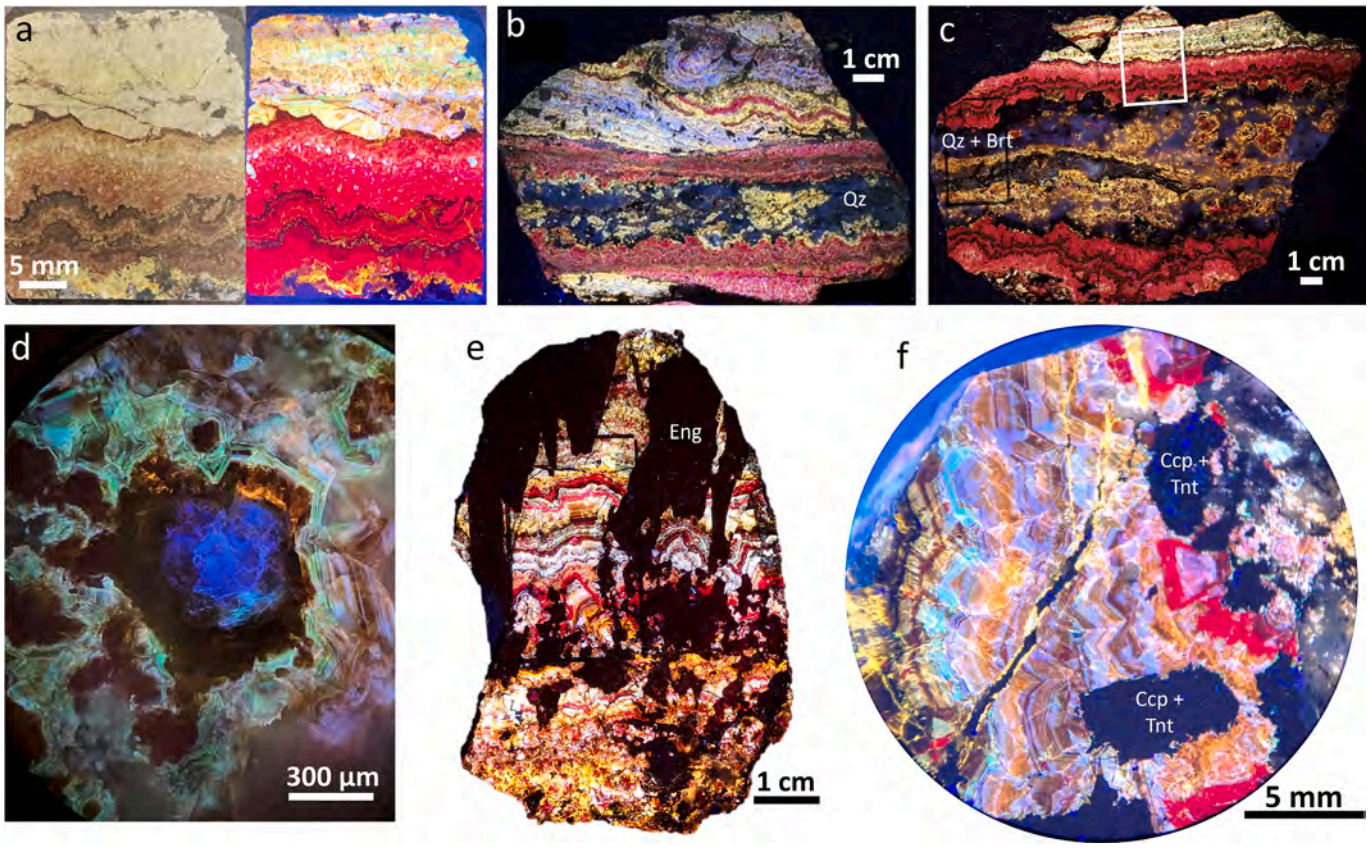

Fig. 4. Photographs showing photoluminescent sphalerite under natural light (a) and 365 nm longwave UV light (a, b, c, d, e, and f). Samples are predominantly sphalerite with other minerals labeled: quartz (Qz), barite (Brt), chalcopyrite (Ccp), tennantite (Tnt), or enargite (Eng). In these specimens, light green sphalerite fluoresces yellow, green, and blue, whereas darker olive-brown sphalerite fluoresces bright red. a) Close-up views of the CB-TF-01 sample (see rectangle in panel c) under visible and long wave UV light; b) Scratch Awl CB-SA-04; c) True Fissure CB-TF-01; d) Close-up of Trout Mine B sample; e) Scratch Awl CB-SA-03; f) microscope view of Scratch Awl CB-SA-04. (For interpretation of the references to color in this figure legend, the reader is referred to the web version of this article.)

3. Results

3.1. Textures and paragenesis

The most vividly fluorescent sphalerites are located in veins in the center of the Philipsburg district, including the Scratch Awl, True Fissure, Algonquin, and Trout mines (Fig. 2). Amongst the fluorescent samples, two types of sphalerites can be distinguished: a brown-colored variety fluorescing bright crimson-red to dark brownish red, and a pale olive-green variety fluorescing blue, green, and yellow (Fig. 4a.). The long-wave UV lamp reveals very detailed and delicate growth bands within sphalerite grains that are not visible in ambient light and are

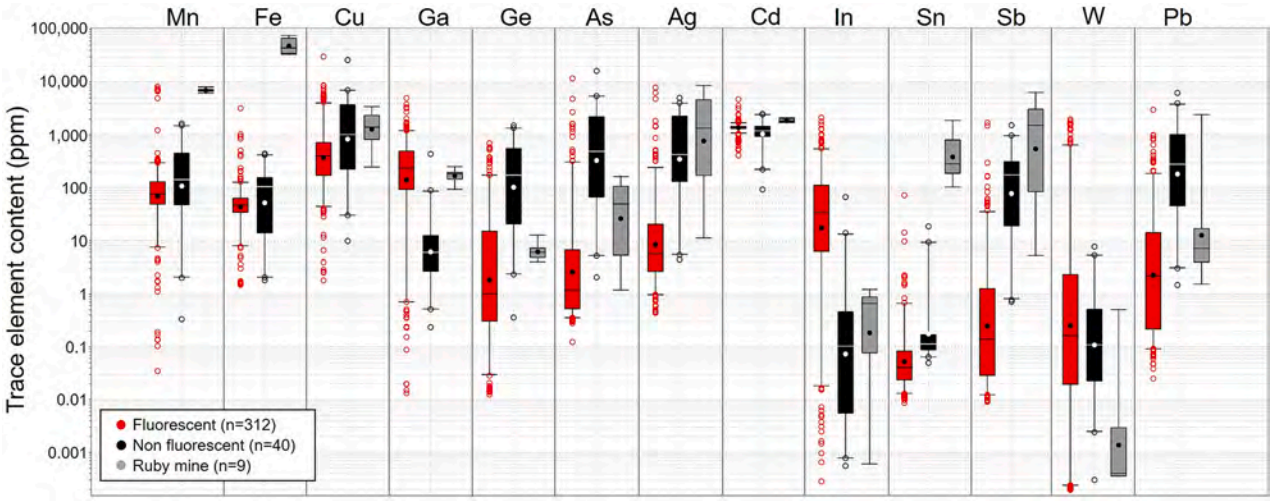

Fig. 5. Percentile box plots of trace element content (in ppm) in fluorescent vs. non-fluorescent samples from the Philipsburg mining district. Data from the Ruby Mine are separated from the other non-fluorescent samples. Box = middle 50 % of the data from Q1 to Q3, line in the box = median, dot in the box = mean, whiskers = 5th and 95th percentile, circles outside the whiskers = outlier (top and bottom 5 % of the data).

Table 1
Minimum, median, average, and maximum values of each sample, rounded to three significant figures. Values are in ppm. In parentheses, n is the number of analyses. Values preceded by the "<" symbol are the detection level, indicating that the measured values were below the detection limit. Samples origin: SA=Scratch Awl mine, TF=True Fissure mine, 2P=Two Percent mine, AL=Algonquin mine, TR=Trout mine, DR=Durango mine, RB=Ruby (Granite Bi-Metallic) mine, SF=San Francisco mine. More details on sample locations are given in electronic appendix 4.

Samples		Mn	Fe	Cu	Zn	Ga	Ge	As	Ag	Cd	In	Sn	Sb	W	Pb	Bi
SA-04(n = 52)	min	31.7	21.7	47.7	651,000	38.2	<0.0261	0.693	0.973	1060	1.44	<0.0174	<0.0180	<0.000473	0.0598	<0.00915
	med	88.4	47.6	524	667,000	261	1.08	1.54	5.78	1420	63.3	0.0314	0.231	0.881	2.36	0.676
	Av	**105**	**87.2**	**1470**	**665,000**	**525**	**42.7**	**108**	**16.2**	**1450**	**203**	**0.0742**	**1.68**	**176**	**23.7**	**10.9**
	max	264	1030	8670	668,000	5000	296	4820	102	1950	1300	0.520	24.7	1570	413	225
SA-22(n = 72)	min	24.9	24.8	37.5	649,000	27.9	<0.0236	0.279	0.441	1260	0.240	<0.0400	<0.0501	<0.000377	0.0837	<0.00783
	med	61.0	47.4	357	667,000	304	0.374	0.460	1.70	1350	37.9	<0.0483	<0.0713	0.0700	0.120	<0.0106
	Av	**73.9**	**56.4**	**423**	**666,000**	**378**	**2.26**	**0.894**	**2.28**	**1370**	**68.5**	**<0.0492**	**0.281**	**1.15**	**1.12**	**0.129**
	max	229	150	1170	667,000	1210	46.4	10.4	9.12	1600	308	0.251	5.94	17.7	38.5	1.54
SA-35(n = 74)	min	41.9	31.0	37.6	663,000	27.6	<0.0212	0.301	1.21	1250	0.536	<0.0246	<0.0238	<0.000375	0.0948	<0.00781
	med	90.7	54.2	416	667,000	338	0.808	0.616	4.33	1350	35.7	<0.0362	<0.0378	0.0944	1.73	0.186
	Av	**102**	**55.4**	**485**	**667,000**	**351**	**6.39**	**1.69**	**5.90**	**1380**	**93.9**	**0.0780**	**0.295**	**21.4**	**4.03**	**2.15**
	max	255	107	2830	668,000	1050	122	28.3	20.2	2360	1570	1.57	5.73	736	28.1	109
TF-03(n = 47)	min	34.1	21.0	146	617,000	73.4	0.100	1.39	5.88	1110	1.14	<0.0174	0.0176	0.0227	0.270	0.00736
	med	141	47.5	556	666,000	374	8.11	6.08	21.3	1360	96.8	<0.0368	1.23	3.24	15.5	1.54
	Av	**190**	**75.1**	**2410**	**663,000**	**727**	**67.7**	**334**	**34.1**	**1360**	**245**	**0.0822**	**5.86**	**356**	**32.2**	**7.42**
	max	1230	849	30,400	667,000	3370	584	11,800	322	1850	2130	0.684	53.4	1980	316	47.6
2P-14(n = 6)	min	4950	203	271	647,000	62.1	0.905	92.2	53.6	1480	3.05	1.65	12.2	0.0192	52.2	0.0101
	med	7060	314	1040	656,000	142	20.9	532	1090	1550	5.76	5.93	180	0.0793	206	0.0714
	Av	**6930**	**792**	**1310**	**655,000**	**129**	**25.0**	**750**	**2770**	**1560**	**5.57**	**17.0**	**598**	**1.32**	**724**	**1.38**
	max	8190	3200	2930	663,000	182	61.9	1630	7900	1690	9.13	72.2	1700	7.54	3000	7.80
AL-103(n = 19)	min	23.9	11.2	6.55	668,000	0.352	0.383	0.644	3.93	1290	0.0193	0.0746	<0.0300	0.00760	0.0251	<0.00212
	med	49.8	24.9	274	669,000	59.9	1.47	1.18	21.3	1500	12.1	0.109	0.0514	0.452	3.07	0.0363
	Av	**89.2**	**25.2**	**314**	**669,000**	**104**	**32.2**	**2.42**	**28.4**	**1490**	**150**	**0.371**	**0.435**	**14.3**	**4.31**	**0.0400**
	max	327	59.2	1330	669,000	357	337	13.0	118	1660	746	2.27	2.81	196	20.5	0.109
TR-01(n = 29)	min	<0.0687	1.50	1.81	657,000	0.0133	<0.0274	0.123	0.470	411	<0.000527	0.0468	0.00925	<0.000368	0.0384	<0.00173
	med	7.27	7.67	117	669,000	7.17	37.1	10.4	16.8	1280	0.0854	0.0777	2.49	0.0720	6.91	0.00416
	Av	**9.19**	**18.0**	**282**	**668,000**	**45.3**	**42.5**	**121**	**275**	**1520**	**3.65**	**0.0766**	**20.5**	**0.565**	**117**	**0.0435**
	max	36.7	107	1890	670,000	448	164	1290	4820	4730	34.2	0.0956	167	4.41	995	0.759
DR-02(n = 13)	min	15.1	15.3	35.4	663,000	0.0198	0.495	4.22	45.5	545	<0.00188	0.0814	1.07	<0.000800	20.0	<0.00203
	med	63.7	34.2	236	668,000	1.03	30.7	109	208	1190	0.410	0.192	18.1	0.0301	94.9	0.00605
	Av	**71.1**	**74.6**	**606**	**667,000**	**7.77**	**157**	**288**	**373**	**1180**	**2.10**	**0.298**	**25.7**	**0.0392**	**187**	**0.0245**
	max	142	428	1850	670,000	52.9	696	1430	1490	1990	10.4	1.47	83.0	0.132	868	0.102
All fluorescent samples	min	**<0.0375**	**1.50**	**1.81**	**617,000**	**0.0133**	**<0.0212**	**0.123**	**0.441**	**411**	**<0.000527**	**<0.0174**	**<0.0138**	**<0.000218**	**0.0251**	**<0.00156**
	med	**76.3**	**47.2**	**402**	**667,000**	**235**	**1.01**	**1.18**	**5.68**	**1370**	**33.9**	**0.0405**	**0.141**	**0.163**	**2.19**	**0.0821**
	Av	**227**	**62.4**	**899**	**666,000**	**373**	**31.1**	**102**	**87.0**	**1390**	**117**	**0.491**	**14.7**	**86.9**	**32.4**	**3.12**
	max	**8190**	**1030**	**30,400**	**670,000**	**5000**	**696**	**11,800**	**7900**	**4730**	**2130**	**72.2**	**1700**	**1980**	**995**	**225**
RB-05a(n = 9)	min	6200	33,700	247	580,000	93.4	4.06	1.19	11.2	1720	<0.00106	103	5.23	<0.000695	1.54	<0.000606
	med	6990	44,400	1400	611,000	183	6.03	49.5	1340	1850	0.667	283	1510	0.000732	7.13	0.00134

(*continued on next page*)

Table 1 (*continued*)

Samples		Mn	Fe	Cu	Zn	Ga	Ge	As	Ag	Cd	In	Sn	Sb	W	Pb	Bi
	Av	**7020**	**50,900**	**1610**	**601,000**	**174**	**6.51**	**60.5**	**2480**	**1900**	**0.522**	**572**	**1960**	**0.0575**	**277**	**<0.00176**
	max	8100	76,400	3440	621,000	252	12.7	163	8660	2110	1.22	1880	6390	0.507	2420	<0.00413
SF-27(n = 6)	min	0.335	2.06	201	660,000	0.236	4.67	58.3	138	1400	0.000943	0.0903	214	0.00445	76.0	0.00135
	med	6.27	21.6	878	665,000	5.39	45.5	287	672	2000	0.00450	0.157	792	0.0297	346	0.0162
	Av	**151**	**50.7**	**1060**	**665,000**	**8.09**	**112**	**445**	**978**	**1990**	**0.438**	**1.61**	**767**	**0.0449**	**471**	**0.0170**
	max	874	146	2660	668,000	21.0	396	1450	3140	2500	2.58	8.72	1530	0.129	1490	0.0404
SA-25(n = 12)	min	7.35	<3.06	96.9	647,000	0.650	9.38	17.1	15.1	92.6	0.0416	0.0903	4.60	0.00243	13.7	<0.000979
	med	316	11.2	2800	665,000	10.5	404	592	609	834	1.14	0.149	155	0.0679	276	0.00275
	Av	**546**	**14.8**	**2850**	**661,000**	**56.6**	**574**	**1780**	**1210**	**772**	**7.94**	**2.49**	**191**	**1.49**	**783**	**0.0122**
	max	1640	49.7	5780	669,000	436	1510	5450	4040	1360	66.7	18.6	568	7.68	3990	0.0477
TF-106(n = 22)	min	36.7	39.2	9.82	619,000	0.515	0.360	2.07	4.47	860	<0.000877	0.0495	0.715	<0.000338	1.48	<0.000686
	med	180	150	915	667,000	3.99	140	424	242	1160	0.0571	0.0904	58.9	0.252	215	0.00182
	Av	**224**	**189**	**2840**	**663,000**	**7.04**	**270**	**1770**	**1130**	**1220**	**0.113**	**0.129**	**142**	**0.533**	**709**	**<0.00300**
	max	527	443	26,200	669,000	28.0	906	16,300	5020	1850	0.581	0.401	577	5.25	6250	0.00736
All non fluorescent samples	min	**0.335**	**1.82**	**9.82**	**580,000**	**0.236**	**0.360**	**1.19**	**4.47**	**92.6**	**<0.000877**	**0.0495**	**0.715**	**<0.000338**	**1.48**	**<0.000606**
	med	**252**	**115**	**965**	**663,000**	**9.08**	**55.7**	**163**	**309**	**1320**	**0.0977**	**0.130**	**181**	**0.0432**	**136**	**0.00182**
	Av	**1510**	**9050**	**2240**	**650,000**	**48.1**	**263**	**1200**	**1170**	**1270**	**2.13**	**101**	**405**	**0.600**	**585**	**0.00583**
	max	**7370**	**76,400**	**26,200**	**669,000**	**436**	**1510**	**16,300**	**5020**	**2500**	**66.7**	**1880**	**4530**	**5.29**	**6250**	**0.0477**

subdued or absent using conventional optical microscopy. Specimens from two mine shafts located 0.5 km apart show similar growth-band patterns (Fig. 4b and c), suggesting a type of sphalerite stratigraphy as described by McLimans et al. (1980). Blue, green, and pale yellow fluorescent bands display a phosphorescent glow for roughly one second after the UV lamp is turned off. The fluorescent sphalerite is also triboluminescent, a phenomenon where light is emitted by mechanical stimuli, and emits orange sparks when scratched with a nail or cut with a saw blade (Beaucamp, 2024).

Other minerals associated with fluorescent sphalerite in the mines of the central district include enargite, tennantite-(Zn), galena, minor pyrite and chalcopyrite, trace huebnerite, and a gangue of quartz + rhodochrosite with trace fluorite. Paragenetic studies from Prinz (1967) indicate a single period of mineralization for the main hypogene sulfides. The tennantite is notably rich in zinc and poor in antimony, with an average chemical formula of $Cu_{10}(Zn_{.86}Fe_{.10}Pb_{.04})_2As_4S_{13}$ based on LA-ICP-MS analysis (see below). Tennantite characteristically occurs along boundaries between enargite and sphalerite. To the south, sphalerite in the important Granite-Bimetallic (Ruby) mine, the largest silver producer in the district, is non-fluorescent and has abundant spherical inclusions of chalcopyrite (chalcopyrite disease). Chalcopyrite inclusions are not present in the fluorescent sphalerite despite the abundance of coexisting Cu-As sulfides in the veins. Other primary sulfide minerals in the Ruby samples include galena, pyrite, arsenopyrite, Ag-rich tetrahedrite, proustite-pyrargyrite, minor huebnerite, and stibnite, with a gangue of quartz + rhodochrosite. Supergene enrichment of silver played an important role in upgrading the tenor of the veins of the Philipsburg district (Emmons and Calkins, 1913). Supergene minerals, including acanthite and elemental silver, replaced primary sulfides to form pockets of extremely high-grade ore, which, for a brief period, made Philipsburg one of the richest silver producers worldwide.

3.2. *LA-ICP-MS analysis of sphalerite*

The complete database of LA-ICP-MS spot analyses obtained in this study is available in the electronic appendix 2. Box plots summarizing distributions of content of selected elements are shown in Fig. 5, and summary statistics arranged by mine of origin are given in Table 1. The data are separated into three categories: fluorescent sphalerite from the central zone of the district (n = 312), non-fluorescent sphalerite from the central zone of the district (n = 40), and non-fluorescent sphalerite from the Ruby Shaft (Granite-Bimetallic mine; n = 9). The first two categories were separated to see if there were clear trends in trace element content that might explain the presence or absence of UV-luminescence across the district.

Fluorescent sphalerite from the district's center has a very low Fe concentration (≤100 ppm – Table 1). This is consistent with the reported inhibition effect of iron on the luminescence of natural and synthetic sphalerite (e.g., Saleh et al., 2019). However, non-fluorescent sphalerites from the same veins have a similar range in Fe concentration. This suggests that other metals besides Fe must play a role in suppressing or enhancing UV fluorescence. Metals enriched in fluorescent sphalerite include Ga and In, whereas non-fluorescent sphalerite is enriched in Ge, As, Ag, Sb, and Pb. Concentrations of Mn, Cu, and Cd are similar. Although most sphalerite samples from Philipsburg contain low concentrations of W (<1 ppm), sphalerite that fluoresces deep red has highly anomalous W up to and exceeding 1000 ppm. Laser-ablation profiles show no evidence of solid inclusions of W-bearing minerals (see examples in the electronic appendix 3), suggesting that the W is present in solid solution in the ZnS lattice. Sphalerite from the Ruby (Granite-Bimetallic) mine differs from sphalerite in the central zone in many respects, including having much higher Mn and Fe contents, higher Sn and Sb, slightly higher Cu and Ag, and lower W. Concentrations of Ga, Ge, As, Cd and Pb in Ruby sphalerite are similar to those in fluorescent sphalerite from the central zone. The average Ag content of Ruby sphalerite (2480 ppm) is remarkably high, making this mineral an

Table 2
Summary of LA-ICP-MS spot analyses of tennantite and enargite coexisting with fluorescent sphalerite from the Scratch Awl and True Fissure mines. (Average, median, maximum, and minimum values shown).

	Wt%		ppm											
	Cu	As	Fe	Zn	Ga	Ge	Ag	Cd	In	Sb	Te	W	Tl	Pb
Tennantite (n = 104)														
avg	38.1	17.2	9170	90,500	46	570	1960	319	30	4560	123	171	523	13,300
med	38.4	17.3	5400	98,800	35	380	1550	251	10	3910	68	42	290	3460
max	42.1	21.3	40,700	141,000	184	10,500	7640	2520	341	36,300	1780	1370	5800	89,800
min	31.8	13.5	111	26,400	2	7	458	44	0	41	2	0	4	244
Enargite (n = 22)														
avg	47.4	19.2	1060	964	1	456	475	11	0	4330	156	6	8	154
med	47.4	19.3	126	487	0	329	79	8	2	4640	70	0	2	23
max	50.1	20.7	4140	4440	8	2450	2620	37	8	9080	598	54	41	896
min	45.2	16.3	10	10	0	40	5	1	0	215	5	0	0	1

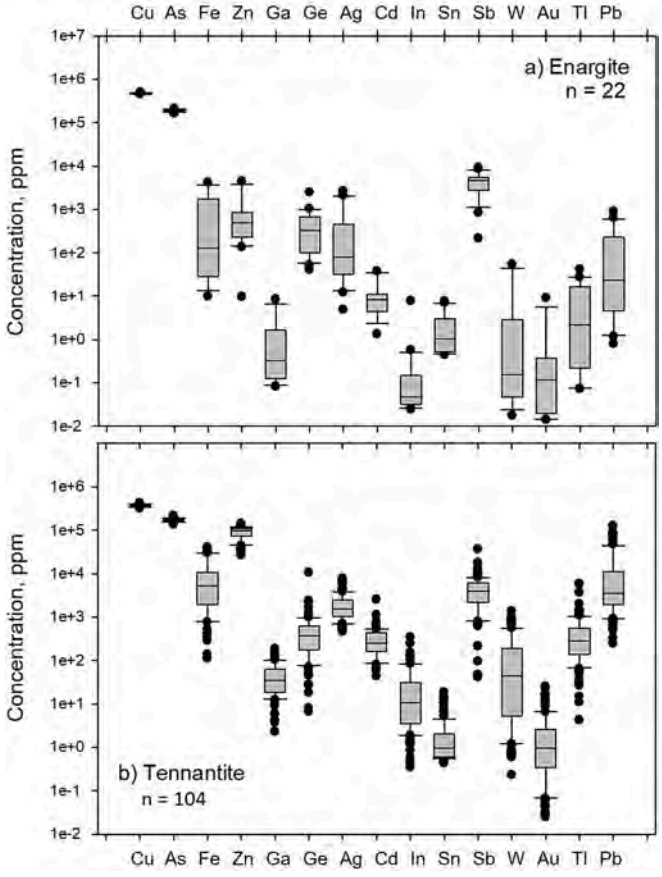

Fig. 6. Trace element contents of a) enargite and b) tennantite coexisting with fluorescent sphalerite (LA-ICP-MS analyses). Outliers are < 5th and > 95th percentile.

important host for Ag.

3.3. LA-ICP-MS analysis of tennantite and enargite

The chemical compositions of tennantite and enargite coexisting with fluorescent sphalerite from the Scratch Awl and True Fissure mines are summarized in Table 2 and Fig. 6. The tennantite is rich in Zn (avg. 9.1 wt%) and Pb (avg. 1.3 %), along with Ge (avg. 570 ppm, max 1.1 %), Ag (avg. 1960 ppm, max. 7640 ppm), W (avg. 171 ppm), and Tl (avg. 523 ppm). Compared to tennantite, enargite has similar Ge (avg. 456 ppm), lower Ag, and much lower Zn, Tl, and Pb concentrations. The average As/Sb mass ratio for both minerals is similar (38 for tennantite, 44 for enargite). Overall, the trace element concentrations reported here for tennantite and enargite fall within the ranges reported for these minerals in previous studies employing LA-ICP-MS methods (George et al., 2017; Liu et al., 2019).

3.4. Raman spectroscopy

Fluorescent sphalerites from Philipsburg exhibit systematic shifts in their Raman spectra that correlate to the color they display under long-wave UV irradiation (Fig. 7). Sphalerite grains that fluoresce in the blue, green, or yellow range exhibit a single sharp Raman peak at 349 cm^{-1} corresponding to pure sphalerite. In contrast, sphalerite that fluoresces pink, violet, or deep red exhibits a second peak at 427 cm^{-1} that eventually exceeds the 349 cm^{-1} peak in intensity for the darkest red luminescent samples. As discussed below, the red fluorescence and the shift in Raman peaks are most closely correlated to the presence of tungsten (W data are included in Fig. 7).

4. Discussion

4.1. Inter-element correlations

Trace elements can enter sphalerite as inclusions of micron- or submicron-sized mineral particles or as a solid solution within the ZnS crystal lattice. LA-ICP-MS element concentration maps in Fig. 8 summarize the spatial distributions of Cu, Ga, Ge, Hg, Cd, In, W, and Ag over a 1.5 x 3.6 mm area within a zoned, fluorescent sphalerite sample from Philipsburg. The results reveal sharp and consistent correlations between UV-fluorescence bands and the concentrations of several trace elements. The similarity of the Cu and Ga maps is particularly striking. Such delicate banding is evidence against the random incorporation of solid mineral inclusions. Furthermore, mineral inclusions were uncommon based on examination of the laser ablation profiles: fewer than 10 % of the laser spots showed clear evidence of such anomalies, in which case the data were discarded for further data treatment. Fig. 8 includes an inset of the 1.0 x 3.2 mm area analyzed with hyperspectral cathodoluminescence (HCL). The position of the energy bands on the HCL map correlates with some elements in the LA-ICP-MS maps, such as Cu, as well as several of the UV-fluorescent bands.

Linear correlations between the concentrations (in units of atomic ppm) of selected pairs of elements in Philipsburg sphalerites are summarized in Fig. 9. Copper is positively correlated with several metals, including Ga, W, In, Ge, and As, whereas Ag is most strongly correlated with Sb and As. Possible reasons for these inter-element correlations are discussed in the next section.

4.2. Mechanisms for trace element incorporation into sphalerite

Trace elements with a prevalent +2 oxidation state, such as Fe, Mn,

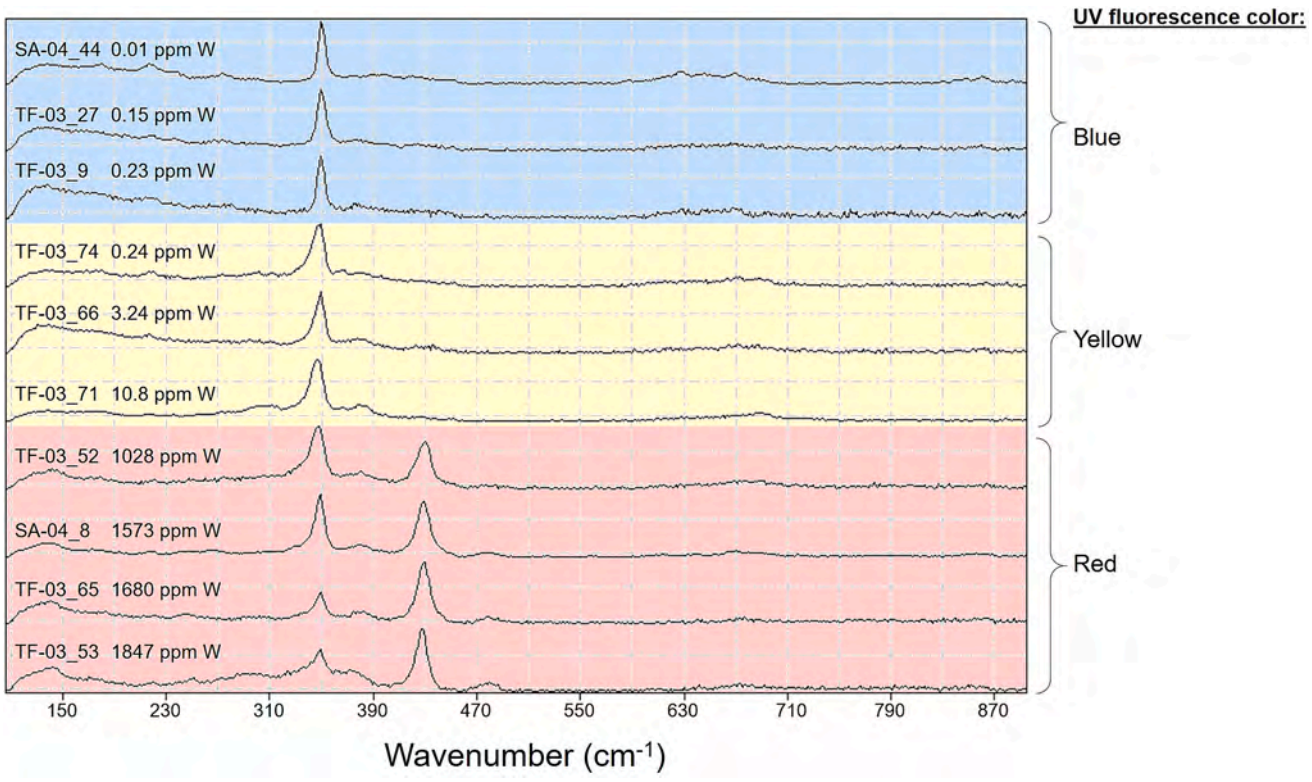

Fig. 7. Raman spectra for selected growth bands in fluorescent sphalerite from Philipsburg. The color of UV fluorescence is given on the right, and the tungsten concentration determined by LA-ICP-MS is indicated next to each spectrum.

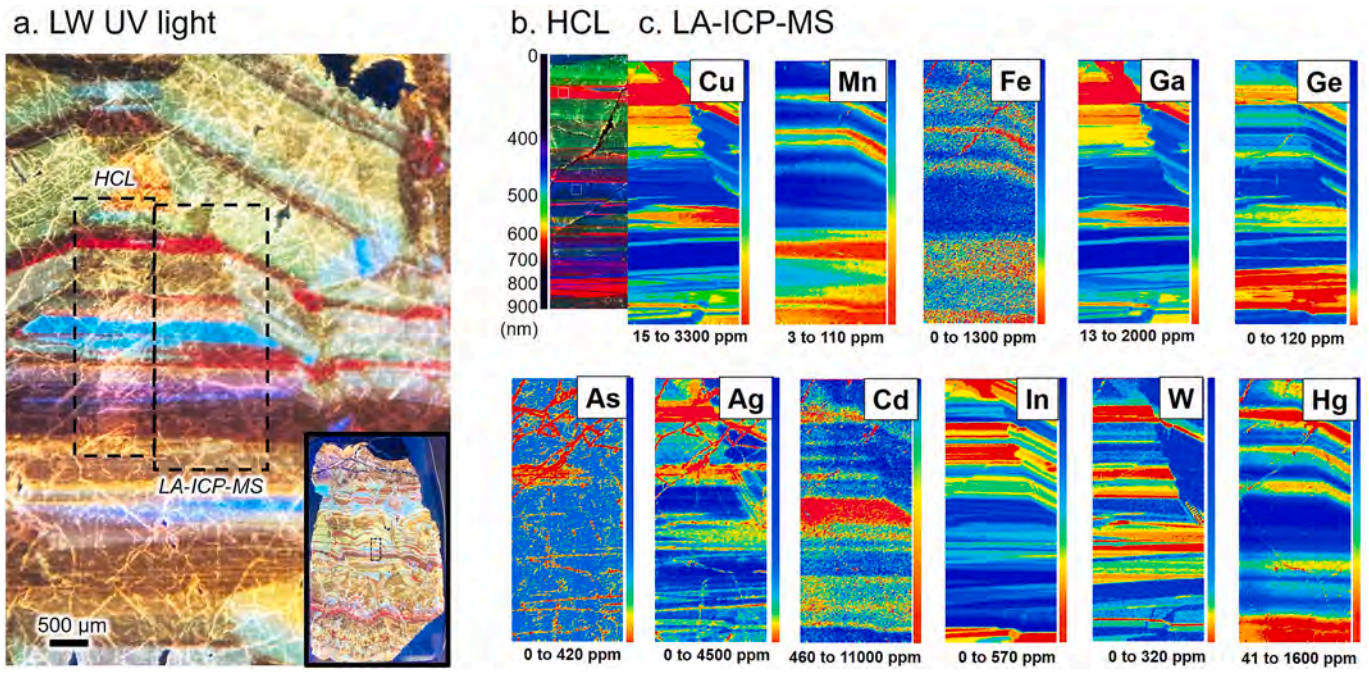

Fig. 8. LA-ICP-MS elemental mapping of one small area of a thin section from Sample CB-SA-22 from the Scratch Awl mine. a) Sample CB-SA-22 as it appears under longwave UV light; b) HCL false-color map shown in Fig. 3; c) Single-element heat maps obtained by LA-ICP-MS area mapping: false colors range from blue (low) to red (high) based on relative concentration (ranges in ppm are shown below each metal map). Dashed lines in the UV light image indicate the HCL and LA-ICP-MS scans' locations. (For interpretation of the references to color in this figure legend, the reader is referred to the web version of this article.)

Cd, and Pb, can substitute for zinc in a simple substitution reaction $ZnS + M^{2+} = MS + Zn^{2+}$, where M represents the abovementioned elements. Partitioning of any divalent metal into sphalerite can be described by a simple distribution coefficient (D_M) relation:

$$[M/Zn]_{sph} = D_M{}^{*}[M/Zn]_{fluid} \quad (1)$$

The relatively small variation in Cd content of sphalerites from across

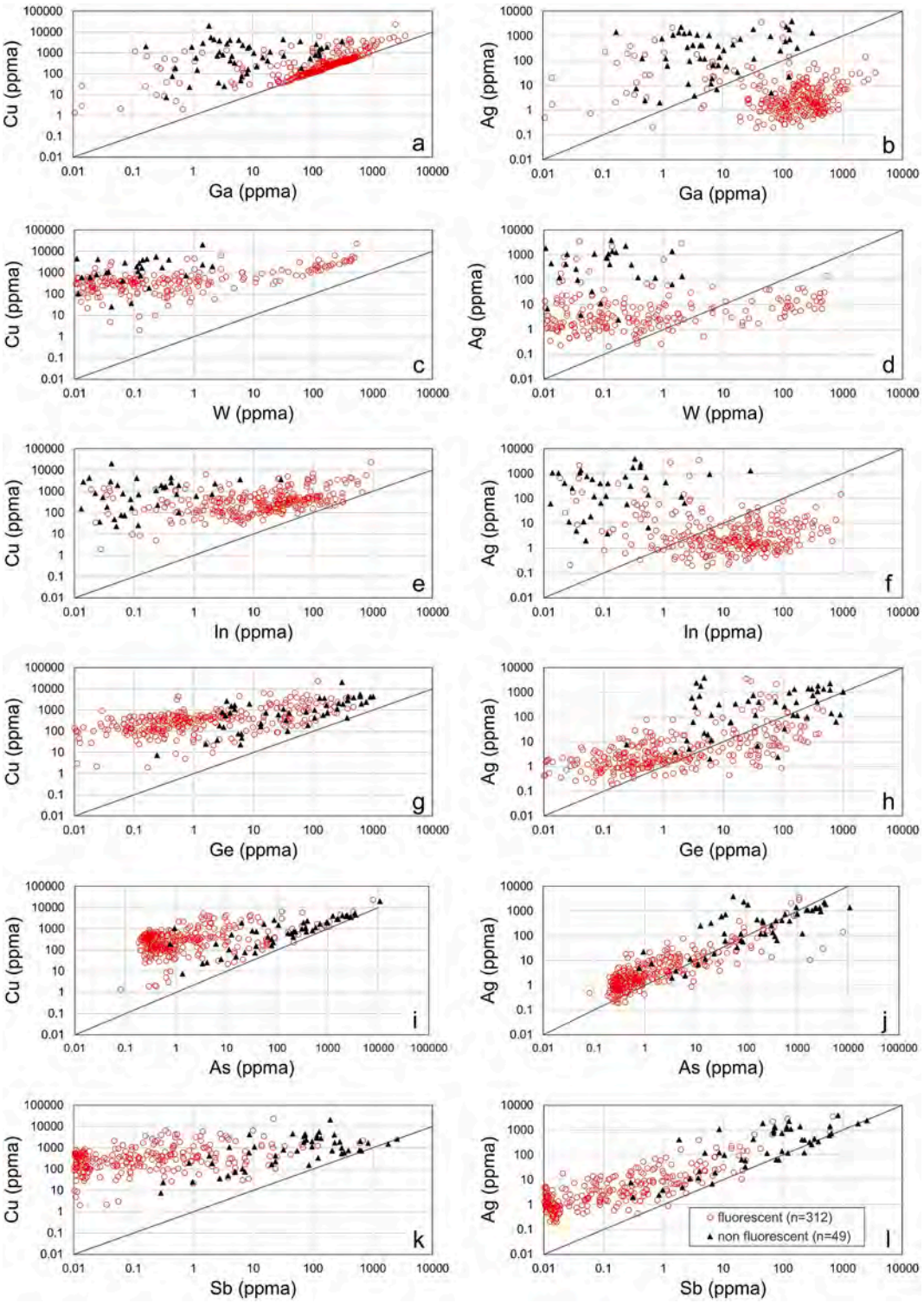

Fig. 9. Correlation of selected elements with Ag and Cu in ppma (atomic content in ppm) from the LA-ICP-MS spot analyses of all twelve samples listed in Table 1. The 1:1 line is shown in each panel for comparison.

the district (Fig. 5) and across growth bands in individual sphalerite grains implies that the Cd/Zn ratio of the ore fluids was nearly constant, and that the value of D_{Cd} must be close to unity. This is somewhat surprising, considering that the ion radius of Cd^{2+} is roughly 24 % larger than the radius of Zn^{2+} (Table 3). Unlike Cd, partitioning of Mn, Fe, and Pb into sphalerite is complicated by the ability of these metals to form sulfide (Fe, Pb) or carbonate minerals (Mn), and indeed Fe, Mn, and Pb show a higher variance compared to Cd in the data (Fig. 5). Rhodochrosite is abundant in the veins of Philipsburg, and the Mn-content of sphalerite is likely influenced by the following reaction:

$$MnS_{sph} + H_2O + CO_2 = MnCO_3(s) + H_2S(aq) \quad (2)$$

where MnS_{sph} refers to the MnS component in the sphalerite host. Thus, although Mn^{2+} and Zn^{2+} have similar chemistry, the Mn/Zn ratio would not be expected to be constant across the district due to spatial or temporal changes in the H_2S/CO_2 ratio. Some degree of variance could

Table 3
Crystal radii (units of picometer, pm) for selected cations arranged according to valence (data from Shannon, 1976). The suffixes "ls" and "hs" refer to low spin and high spin states. All radii assume octahedral coordination unless specified otherwise, i.e., (4) = tetrahedral. Cations in bold are considered to have a higher likelihood of substituting into sphalerite under the geologic conditions at Philipsburg.

Valence	1^+	2^+	3^+	4^+	5^+	6^+
Mn ls		**81**	72	67	47 (4)	39.5 (4)
Mn hs		**97**	78.5			
Fe ls		**75**	69	72.5		39 (4)
Fe hs		**92**	78.5			
Pb		**133**		91.5		
Cd		**109**				
Cu	**91**	**87**	68 ls			
Ag	**129**	108	89			
Ga			**76**			
In			**94**			
Sn				**83**		
As			**72**		60	
Sb			**90**		74	
Bi			**117**		90	
Ge		87		**67**		
W				80	76	**74**
Zn		**88**				

also be attributed to exchange reactions with a D_i value that differs from unity. For example, the crystal radius of Pb^{2+} is much greater than that of Zn^{2+} (51 % mismatch, Table 3), suggesting that the D_{Pb} value is likely to be less than unity.

The incorporation of trace elements with a valence other than +2 into sphalerite can be accommodated by a site vacancy or coupled substitutions. For example, the incorporation of In^{3+} into sphalerite could be written this way:

$$2In^{3+} + 3ZnS = 2InS_{sph} + \square S_{sph} + 3Zn^{2+} \quad (3)$$

where the symbol □ indicates a cation-site vacancy. Alternatively, In^{3+} could enter the sphalerite structure as a coupled substitution with a univalent metal, such as Cu^+ or Ag^+ (Cook et al., 2009; Frenzel et al., 2016):

$$In^{3+} + Cu^+ + 2ZnS = InS_{sph} + CuS_{sph} + 2Zn^{2+} \quad (4)$$

Other trivalent elements that could substitute in this fashion include Ga, Sb, As, and Bi.

In the case of Ge, Sn, and W, it is not obvious which valence state(s) may be prevalent in the sphalerite structure. Recent studies employing synchrotron methods (i.e., XANES) have shown that both Ge^{2+} and Ge^{4+} can be present in sphalerite (Hayes et al., 2023; Liu et al., 2023). As shown in Table 3, Ge^{2+} has a crystal radius of 87 pm that is a better match for Zn^{2+} compared to Ge^{4+} (67 pm). Likewise, previous workers have proposed the presence of Sn^{2+} and/or Sn^{4+} in sphalerite and wurtzite (e.g., Pring et al., 2020). Incorporation of a tetravalent species by coupled substitution with copper can be written as follows:

$$M^{4+} + 2Cu^+ + 3ZnS = MS_{sph} + 2CuS_{sph} + 3Zn^{2+} \ (M = Ge, Sn) \quad (5)$$

In this study, we observe a weak correlation of Ge with Cu (Fig. 9), suggesting that at least some germanium has a valence of +4 and substitutes for Zn^{2+} with the help of Cu^+.

The substitution of tungsten into sphalerite is an especially interesting case. Tungsten concentrations are highly elevated (up to 1980 ppm) in the brightest-red fluorescent sphalerite bands from Philipsburg. The most common oxidation state of tungsten in the earth's crust is +6, although W^{+4} is present in the rare sulfide mineral tungstenite, WS_2. As discussed by Hsu (1977), the rarity of tungstenite compared to its analog molybdenite (MoS_2) is explained by the strongly reducing conditions required to convert W^{+6} to W^{+4}. The coexistence of coeval barite and enargite with W-rich sphalerite in the veins of the central Philipsburg district argues against strongly reducing conditions. Therefore, we argue that tungsten likely entered sphalerite in the hexavalent valence state. Both W^{4+} and W^{6+} have crystal radii that are within 15 % of the radius of Zn^{2+} (Table 3).

The following equations summarize possible substitution reactions that could take place within Philipsburg sphalerite:

$$M^{2+} \leftrightarrow Zn^{2+} \quad for\ M = Fe,\ Mn,\ Cd,\ Hg,\ Pb \quad (6)$$

$$A^+ + M^{3+} \leftrightarrow 2Zn^{2+} \quad for\ M = Ga,\ In,\ As,\ Sb,\ Bi\ and\ A = Cu,\ Ag \quad (7)$$

$$2A^+ + M^{4+} \leftrightarrow 3Zn^{2+} \quad for\ M = Ge\ and\ A = Cu,\ Ag \quad (8)$$

$$4A^+ + M^{6+} \leftrightarrow 5Zn^{2+} \quad for\ M = W\ and\ A = Cu,\ Ag \quad (9)$$

All of these reactions are written with balanced charges and an equal number of metal cations on both sides, thus avoiding the need for vacancies. If reactions (7), (8), and (9) are indeed the dominant mechanisms for the incorporation of trace metals with a valence other than +2, then it follows that a plot of log (ppma Cu + Ag) vs. log [(ppma Ga + In + As + Sb) + 2x(ppma Ge) + 4x(ppma W)] should have a slope of +1. Fig. 10 shows the resultant stoichiometry plots for Philipsburg sphalerites. Fig. 10a shows all of the LA-ICP-MS spot analyses from different samples across the district, whereas Fig. 10b shows results from the LA-ICP-MS elemental mapping of one small area of a single thin section (Fig. 8). In both cases, the vast majority of the data plot very close to the

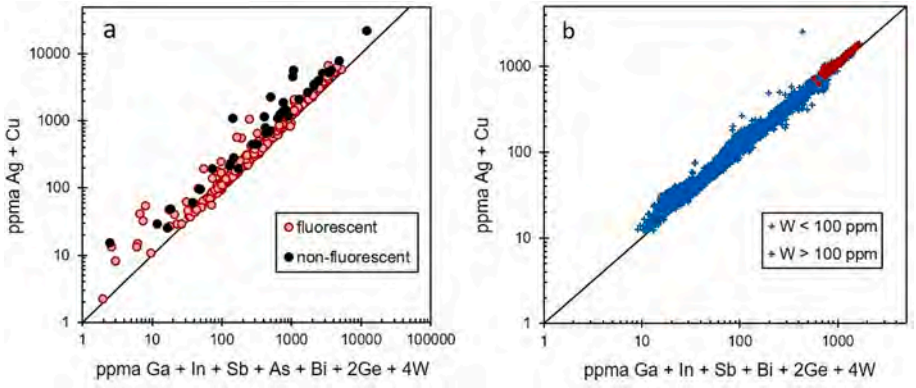

Fig. 10. a) Stoichiometry plot for all sphalerite LA-ICP-MS spot analyses used in this study assuming the coupled substitution model (see text for explanation, ppma = atomic content in ppm). b) Stoichiometry plot of over 40,000 data points from the LA-ICP-MS raster mapping analyses used to create the element heat maps shown in Fig. 8. The diagonal line in both graphs corresponds to the perfect coupled substitution of elements with an oxidation state other than +2 into the sphalerite structure, assuming the reaction stoichiometries discussed in the text.

Table 4
Comparison of ranges of main trace elements in sphalerite from various Cordilleran polymetallic deposits. Value in ppm. IQR=Interquartile range. Some deposits might include data for solid inclusions.

Deposits:	Morococha, Peru (Benites et al., 2021) – *IQR*		Cerro de Pasco (Rottier et al., 2018)[c] – *Range*	Coquiljirca (Ortiz-Benavente et al., 2022) – *Ranges* – *IQR*	Ayawilca (Benites et al., 2022) – *Ranges*	Bingham Canyon, Tomlinson et al., 2021) – *Ranges*	Butte Main Stage veins (Ortelli, 2015) – *Ranges*		Philipsburg, MT (This study) – *Ranges*	
Mineralization type:	Mantos and vein		Mantos and veins	Mantos and veins	Mantos and veins	Veins	Veins		Veins	
Sulfidation state, if applicable:	High[a]	Low[b]		High	Low to intermediate	Intermediate	High (Central)	Low (Peripheral)	Fluorescent	Non fluorescent
Mn	2,120–4,680	2,500–8,500	5.5–3,680		31–4,640	690–2000	8–7,000	8–8,500	0–8,190	0.3–8,100
Fe	85–189	58,000–77,000	200–117,000	16–18	20,000–140,000	15,000–23,000	7–15,000	10–40,000	1.5–3,200	1.8–76,000
Cu	1,770–3,010	42–381	18–1,580	5,200–8,330	6–18,300	3,400–15,300	50–20,000	40–10,000	1.8–30,400	9.8–26,200
Ga	706–1,270	0.14–160	0.5–420	4–13	0.5–92	2.5–64	0.9–700	1–4,000	0–5,000	0.2–436
Ge	1.2–2.0	0.16–0.44	0.2–70	26–63	0.2–14				0–696	0.4–1,510
As	0.33–0.79	0.27–33	0.9–1,420			<10	0.1–300	0.03–200	0.1–11,800	1.2–16,300
Ag	4.2–5.5	2.9–9.9	0.05–740		2.6–195	16–43	0.09–40	1–1,000	0.4–7,900	4.5–8,670
Cd	3,710–4,010	1,760–2,240	470–5,550	1,730–5,410	698–3820	3090–4280	550–2,750	150–7,000	411–4,730	93–2,500
In	726–1,290	23–324	0.25–1450	899–2,780	0.6–2,680	18–255	0.01–600	0.02–15,000	0–2,130	0–67
Sn	1.1–3.4	0.19–15	1–1,160		0.2–15,100	2.3–190	0.8–200	0.3–40	0–72	0–1,880
Sb	0.13–0.40	0.027–0.91	0.08–2,630			1–5.1	0.04–30	0.03–4,000	0–1,700	0.7–6,390
W			0.02–0.12						0–1,980	0–7.7
Pb	1.1–2.6	0.16–1.6	0.03–266,000			3.6–50	0.02–900	0.05–1,500	0–3,000	0.5–6,250

[a] From the Epithermal overprint on the Toromocho porphyry.
[b] From the Porvenir and Manto Italia skarn and mantos.
[c] Note: original data from Rottier et al. (2018) were filtered to remove fluid inclusions.

1:1 line for both fluorescent and non-fluorescent sphalerite types. Data that plot to the left of the 1:1 line can be explained at least two ways: 1) entrainment of sub-microscopic inclusions of chalcopyrite, argentite, or other Cu-Ag-bearing minerals or 2) incorporation of Cu^{2+} in addition to Cu^{+} into the sphalerite lattice. Importantly, no analyses plot far to the right of the 1:1 line, consistent with the lack of any mineral inclusions containing Ga, In, As, Sb, Ge, or W in the sphalerites examined. Overall, the strong linearity of the data conforming to a slope of 1 and the relative lack of outliers is evidence in favor of the coupled substitution model for the incorporation of trace elements into Philipsburg sphalerite.

4.3. Comparison with previous studies

Table 4 summarizes data on the trace element composition of sphalerite from Philipsburg in comparison to other Cordilleran-type, porphyry-lode deposits worldwide (data from Benites et al., 2021, 2022; Rottier et al., 2018; Ortiz-Benavente et al., 2022; Tomlinson et al., 2021; Ortelli, 2015). Although there are differences in how the LA-ICP-MS data were reported amongst the various studies, it is clear that Philipsburg sphalerites have some of the highest concentrations of several elements, including Ga, Ge, Cu, As, Ag, and W. The maximum values of copper in Philipsburg sphalerites exceed 25,000 ppm (>2.5 % Cu), higher than the most Cu-rich sphalerites from Butte and Bingham Canyon, two of the richest porphyry-lode copper deposits in the world. Silver is also exceedingly high in Philipsburg sphalerite, with maximum concentrations in the 7000 – 8000 ppm range, much higher than any other Cordilleran-type deposit, Butte being a distant second place. As discussed in the preceding section, it is likely that both Cu^{+} and Ag^{+} enter the sphalerite lattice in coupled substitution with elements in the +3, +4, or +6 oxidation state. The most important high-valence elements entering Philipsburg sphalerite with Cu and Ag are Ga, As, Ge and W. Tungsten has rarely been reported in previous studies of trace elements in sphalerite. For example, Frenzel et al. (2016) did not mention tungsten in their meta-analysis of sphalerite from 463 localities worldwide. To our knowledge, the only other study to document W in sphalerite is that of Rottier et al. (2018), who reported values up to 0.12 ppm for sphalerite from Cerro de Pasco. These concentrations are orders of magnitude less than at Philipsburg.

In their review of trace elements in sphalerites from Peruvian hydrothermal deposits of varying origin (Cordilleran-type, MVT, VMS, skarns porphyry), Culqui et al. (2022) found that In was enriched in the higher temperature deposits proximal to porphyry intrusions. In contrast, Ge and Ga were enriched in lower-temperature deposits without a direct link to magmatic fluids. The high Ge and Ga and relatively low In concentrations in Philipsburg sphalerites are consistent with a relatively low temperature of formation (i.e., < 210 °C based on fluid inclusion homogenization temperatures, Beaucamp et al., 2022). The sulfidation state may also play a role in trace metal partitioning, as Cordilleran-type deposits are well known for showing district-scale zonation in fS_2-sensitive mineral assemblages. Both Butte and Philipsburg contain high-sulfidation minerals (enargite, low-Fe sphalerite) in the center of the district, zoning outwards to low-sulfidation minerals (tetrahedrite, arsenopyrite, high-Fe sphalerite). However, other than Fe, which is always lower in high-fS_2 conditions, few evident trace-element trends exist when the results of this study are combined with previous work (Table 4). For example, whereas Ga is most enriched in the high-fS_2 veins of Philipsburg and Morococha, the opposite is true at Butte (Ortelli, 2015).

4.4. Possible causes of anomalous fluorescence in Philipsburg sphalerite

Sphalerite is well-known for its ability to fluoresce when exposed to long-wave ultraviolet light, and this property has made synthetic ZnS an essential compound in material science applications (Saleh et al., 2019; Šoster et al., 2023). However, relatively few documented occurrences of strongly fluorescent sphalerite from natural ZnS deposits worldwide

Table 5
Correlation matrix between the height of the observed Raman peaks at 349 and 427 cm^{-1} and the concentrations of associated trace elements (ppm) in fluorescent sphalerite.

	Mn	Fe	Cu	Ga	Ge	As	Ag	Cd	In	Sn	Sb	W	Pb
P1 (349 nm)	−0.03	0.18	−0.3	−0.16	0.11	0.12	−0.17	0.16	−0.37	−0.45	0.27	−0.47	0.19
P3 (427 nm)	−0.17	−0.09	**0.51**	0.27	0.4	−0.09	−0.02	0.15	**0.68**	0.22	−0.2	**0.84**	−0.01

exist. There are at least three possible reasons for this: 1) fluorescent sphalerite is rare; 2) previous workers have not examined their samples with a long-wave UV lamp; or 3) other workers have noted fluorescence but did not consider it important enough to report. Probably the most well-known location for fluorescent sphalerite is Sussex County, New Jersey (Franklin, Sterling Hill mines), where it coexists with several other famously fluorescent minerals (e.g., willemite, franklinite, zincite). Other reported occurrences (from mindat.org) of strongly fluorescent sphalerite include the Sweet Home Mine (Colorado), Bisbee (Arizona), the Horn Silver and Ophir mines (Utah), Balmat (New York), Madison Lead (New Hampshire) and Hasselhojden (Sweden). In a short mineralogical note, Goni and Rémond (1969) described natural sphalerite specimens with strong photoluminescence and cathodoluminescence from several locations worldwide, including the Pb-Zn carbonate-replacement deposits of Djebel Gustar, Algeria. Šoster et al. (2023) recently characterized the UV-fluorescence (photoluminescence) of the Algerian sphalerites in more detail and documented non-fluorescent, orange-yellow, deep red, and bright green luminescence subtypes.

Strongly fluorescent sphalerite requires the presence of an activator (e.g., a trace element or a structural defect) and the absence of fluorescence inhibitors (e.g. Fe, Co). The concentration of the activator need not be high to impart luminescence. Saleh et al. (2019) concluded that photoluminescence in undoped synthetic sphalerite specimens obtained from commercial suppliers was due to the presence of impurities at concentrations as low as 1–2 ppma, and not to intrinsic defects in the mineral lattice. Elements known to activate fluorescence in sphalerite include Cu^{+}, Mn^{2+}, Cd^{2+}, Ga^{3+}, and Ge^{4+} (Goni and Rémond, 1969; Saleh et al., 2019). However, the common co-occurrence of multiple fluorescence activators in natural sphalerite specimens makes assignment of color bands to specific trace elements a difficult task. Šoster et al. (2023) suggested that the coupled substitution of Cu^{+} and Ga^{3+} caused the deep red UV-fluorescence of sphalerite from carbonate-replacement deposits in Algeria. Although this may be the case, it is worth noting that neither Goni and Rémond (1969) nor Šoster et al. (2023) analyzed their sphalerite samples for tungsten.

As shown in Table 5, a positive correlation exists between the height of the 427 cm^{-1} Raman peak and the tungsten concentration of the same growth band as measured by LA-ICP-MS. Although all sphalerite growth bands with high W also have high Cu, the opposite is not the case. Sphalerite with high Cu and Ga (>1000 ppm) but very low tungsten (<10 ppm) shows no trace of a Raman peak at 427 cm^{-1} and does not fluoresce red. Therefore, we tentatively conclude that the 427 cm^{-1} Raman peak and the bright red fluorescence are both mainly attributed to the presence of W in the sphalerite crystal lattice. This idea needs to be tested by synchrotron experiments.

The vivid blue fluorescence of the sphalerite sample from the Trout Mine (Fig. 4d) deserves special mention. The only trace element with elevated concentration (>25 ppm) in the blue-glowing core of this sphalerite grain is Cd (1200–1700 ppm). Also, the blue fluorescent band in Fig. 8 is positively correlated with Cd and negatively correlated with the concentrations of other elements (e.g., Cu, Ga, Ge, Ag, In). It is feasible that the 25 % mismatch in the crystal radii of Cd^{2+} and Zn^{2+} results in lattice strain that manifests itself as photoluminescence.

Understanding which elements or combinations of elements create different colored fluorescence in sphalerite will require the preparation and analysis of synthetic grains doped with controlled mixtures of trace metals, a project that is outside the scope of the present study. This is a worthwhile endeavor, as it may enable rapid screening of sphalerite grains in the field or in a processing circuit for the presence or absence of potentially valuable critical metals (Cu, Ga, In, W, etc). Also, because deeply fluorescent sphalerite requires a low Fe content (usually due to a high fS_2), recognition of this feature in a given Cordilleran polymetallic deposit may provide a vector to the high-sulfidation center of the deposit, when present.

5. Conclusions

This paper has documented the occurrence of unusually colorful fluorescence in sphalerite from the central, high-sulfidation zone of the polymetallic Philipsburg mining district. Fluorescent sphalerite is notably poor in Fe and co-exists with a high-sulfidation mineral assemblage including enargite, tennantite-(Zn), and barite. Sphalerite from Philipsburg's peripheral, Ag-rich veins is Fe-rich, non-fluorescent, and coexists with a low-sulfidation assemblage, including Ag-rich tetrahedrite, galena, and arsenopyrite. Although both types of sphalerite are rich in a variety of trace elements, sphalerite from the peripheral low-sulfidation state Granite-Bimetallic (Ruby) mine has the highest Ag and Sb content and is relatively depleted in Cu, Ga, and W relative to the sphalerite in the center of the district. Robust inter-element correlations provide strong evidence for coupled substitution of univalent Ag and Cu with trivalent Ga, In, Sb, As, and Bi, tetravalent Ge and hexavalent W. Tungsten may be an essential ingredient for sphalerite that fluoresces bright red, and is responsible for a shift in the dominant Raman peak of sphalerite from the usual 349 cm^{-1} to 427 cm^{-1}. Although we propose that tungsten enters the sphalerite lattice as W^{6+} in coupled substitution with Cu^{+}, this needs to be confirmed by other methods (e.g., synchrotron). It is highly recommended that further studies of trace elements in sphalerite include W in the analytical list. It is also recommended that economic geologists and curious academics scan their sphalerite samples with a long-wave UV lamp. The presence or absence of different colors under UV illumination may prove to be a reliable indicator of the presence or absence of different trace elements in sphalerite. Finally, the presence of fluorescent sphalerite co-existing with other high-sulfidation minerals may be a common attribute of the central zone of other Cordilleran polymetallic deposits.

Declaration of competing interest

The authors declare the following financial interests/personal relationships which may be considered as potential competing interests: Christopher H. Gammons reports financial support was provided by National Science Foundation. If there are other authors, they declare that they have no known competing financial interests or personal relationships that could have appeared to influence the work reported in this paper.

Data availability

The dataset used for this research is available in the supplementary material.

Acknowledgments

We thank Gabriel Cangelosi for calling our attention to the fluorescent sphalerite from Philipsburg, and the Antonioli family for

permission to collect samples on their property. The manuscript was improved by reviews by John Dilles, Lisard Torró, Garth Graham, and Chris Mills. Portions of this study were funded by the National Science Foundation (Award 2327676). The first author also thanks the Society for Mining, Metallurgy and Exploration (SME), the Geological Society of America (GSA), the Montana Geological Society (MGS), the American Federation of Mineralogical Society, and the Tobacco Root Geological Society (TRGS) for financial support.

Appendix A. Supplementary data

Supplementary data to this article can be found online at https://doi.org/10.1016/j.oregeorev.2024.106267.

References

Barton, P.B., Toulmin, P., 1966. Phase relations involving sphalerite in the Fe-Zn-S system. Econ. Geol. 61, 815–849. https://doi.org/10.2113/gsecongeo.61.5.815.

Beaucamp, C., Thompson, J., Gammons, C. H., Cangelosi, G., and Lund, K., 2022. Fluorescent sphalerite from Montana, USA: Coupled substitutions of Cu, Ga, and W. Proc. 2022 V.M. Goldschmidt Conf., https://doi.org/10.46427/gold2022.11433.

Beaucamp, C.M., 2024. Trace elements in fluorescent sphalerite from the Philipsburg mining district, Granite County, Montana. In Van Rythoven, A. and Barth, S., eds., 2024, Proceedings of the 2023 Montana Mining and Minerals Symp., Mont. Bur. Mines Geol., Special Publ. 124. p.1-6.

Beaucamp, C., Gammons, C.H., 2022. New investigations of polymetallic lode deposits of Philipsburg, Granite County, Montana. Montana Bur. Mines Geol Special Publ. 123, 131–136.

Benites, D., Torró, L., Vallance, J., Laurent, O., Valverde, P.E., Kouzmanov, K., Chelle-Michou, C., Fontboté, L., 2021. Distribution of indium, germanium, gallium, and other minor and trace elements in polymetallic ores from a porphyry system: the Morococha District. Peru. Ore Geol. Rev. 136, 104236. https://doi.org/10.1016/j.oregeorev.2021.104236.

Benites, D., Torró, L., Vallance, J., Laurent, O., Quispe, P., Rosas, S., Uzieda, M.F., Holm-Denoma, C.S., Pianowski, L.S., Camprubí, A., Colás, V., 2022. Geology, mineralogy, and cassiterite geochronology of the Ayawilca Zn-Pb-Ag-In-Sn-Cu deposit, Pasco Peru. Mineral. Dep. 57, 481–507. https://doi.org/10.1007/s00126-021-01066-z.

Burton, J., 2022. U.S. Geological Survey Releases 2022 List of Critical Minerals. https://www.usgs.gov/news/national-news-release/us-geological-survey-releases-2022-list-critical-minerals.

Catchpole, H., 2011. Porphyry-related polymetallic mineralization in the Morococha district, central Peru: mineralization styles, timing and fluid evolution. Ph.D. dissertation, University of Geneva. https://doi.org/10.13097/archive-ouverte/unige.

Cook, N.J., Ciobanu, C.L., Pring, A., Skinner, W., Shimizu, M., Danyushevsky, L., Saini-Eidukat, B., Melcher, F., 2009. Trace and minor elements in sphalerite: a LA-ICPMS study. Geochim. Cosmochim. Acta 73, 4761–4791. https://doi.org/10.1016/j.gca.2009.05.045.

Culqui, J., Tirado, E., Benites, D., Torró, L., 2022. Trace element contents in sphalerite, chalcopyrite, and galena in ore deposits from Peru –A meta-analysis. In: Christie AB (ed.) Proceedings of the 16th SGA Biennial Meeting, 28-31 March 2022, 1:73–76.

Dilles, J. H., 2004. Geologic field guide to the Butte District. In GSA-SEG Penrose Conference.

Emmons, W. H., and Calkins, F. C., 1913. Geology and ore deposits of the Philipsburg quadrangle, Montana. U.S. Geol. Surv., Prof. Paper 78. .

Fontboté, L., Bendezú, R., 2009. Cordilleran or Butte-type veins and replacement bodies as a deposit class in porphyry systems. In: Proceed. 10th SGA Meeting, pp. 521–553.

Foster, D.A., Grice, W.C., Kalakay, T.J., 2010. Extension of the Anaconda metamorphic core complex: 40 Ar/ 39 Ar thermochronology and implications for Eocene tectonics of the northern Rocky Mountains and the Boulder batholith. Lithosphere 2, 232–246. https://doi.org/10.1130/L94.1.

Foster, D.A., Mueller, P.A., Heatherington, A., Gifford, J.N., Kalakay, T.J., 2012. Lu-Hf systematics of magmatic zircons reveal a Proterozoic crustal boundary under the Cretaceous Pioneer batholith, Montana. Lithos 142–143, 216–225. https://doi.org/10.1016/j.lithos.2012.03.005.

Frenzel, M., Hirsch, T., Gutzmer, J., 2016. Gallium, germanium, indium, and other trace and minor elements in sphalerite as a function of deposit type - a meta-analysis. Ore Geol. Rev. 76, 52–78. https://doi.org/10.1016/j.oregeorev.2015.12.017.

George, L.L., Cook, N.J., Ciobanu, C.L., 2017. Minor and trace elements in natural tetrahedrite-tennantite: effects on element partitioning among base metal sulphides. Minerals 7 (2), 17. https://doi.org/10.3390/min7020017.

Goddard, E. N., 1940. Manganese deposits at Philipsburg, Granite County, Montana, a preliminary report. U.S. Geol. Surv. Bull. 922-G. .

Goldschmidt, V. M., 1930. On the occurrence of germanium in coal and coal products. News from the Göttingen Society of Sciences and Humanities, Mathematical-physical class, 398-402.

Goni, J., Rémond, G., 1969. Localization and distribution of impurities in blende by cathodoluminescence. Mineral. Mag. 37 (286), 153–155. https://doi.org/10.1180/minmag.1969.037.286.01.

Hayes, S.M., McAleer, R.J., Piatak, N.M., White, S.J.O., Seal II, R.R., 2023. A novel non-destructive workflow for examining germanium and co-substituents in ZnS. Front. Earth Sci. 11, 939700. https://doi.org/10.3389/feart.2023.939700.

Holser, W.T., 1950. Metamorphism and associated mineralization in the Philipsburg region Montana. Geol. Soc. Amer. Bull. 61, 1053–1090. https://doi.org/10.1130/0016-7606(1950)61[1053:MAAMIT]2.0.CO;2.

Hsu, L.C., 1977. Effects of oxygen and sulfur fugacities on the scheelite-tungstenite and powellite-molybdenite stability relations. Econ. Geol. 72, 664–670. https://doi.org/10.2113/gsecongeo.72.4.664.

Hyndman, D.W., Obradovich, J.D., Ehinger, R., 1972. Potassium-argon age determinations of the Philipsburg Batholith. Geol. Soc. Amer. Bull. 83 (2), 473–474. https://doi.org/10.1130/0016-7606(1972)83[473:PADOTP]2.0.CO;2.

Liu, W., Cook, N.J., Ciobanu, C.L., Gilbert, S.E., 2019. Trace element substitution and grain-scale compositional heterogeneity in enargite. Ore Geol. Rev. 111, 103004. https://doi.org/10.1016/j.oregeorev.2019.103004.

Liu, W., Mei, Y., Etschmann, B., Glenn, M., MacRae, C.M., Spinks, S.C., Ryan, C.G., Brugger, J., Paterson, D.J., 2023. Germanium speciation in experimental and natural sphalerite: implications for critical metal enrichment in hydrothermal Zn-Pb ores. Geochim. Cosmochim. Acta 342, 198–214. https://doi.org/10.1016/j.gca.2022.11.031.

McLimans, R.K., Barnes, H.L., Ohmoto, H., 1980. Sphalerite stratigraphy of the upper Mississippi Valley zinc-lead district, southwest Wisconsin. Econ. Geol. 75, 351–361. https://doi.org/10.2113/gsecongeo.75.3.351.

Naibert, T.J., Geissman, J.W., Heizler, M.T., 2010. Magnetic fabric, paleomagnetic, and 40Ar/39Ar geochronologic data bearing on the emplacement of the late Cretaceous Philipsburg Batholith. SW Montana Fold-and-Thrust Belt. Lithosphere 2 (5), 303–327. https://doi.org/10.1130/L83.1.

O'Connell, M. P., 2001. Geometry, kinematics, and emplacement mechanisms of the Philipsburg batholith within the Sevier fold-and-thrust belt, Flint Creek Range, western Montana. M.S. Thesis, Montana State Univ., Bozeman, MT.

Oftedal, I.W., 1941. Studies on the minor constituents of mineral minerals from Norwegian zinc blende-bearing deposits. In Commission with J. Dybwad. No. 8.

Ortelli, M., 2015. Polymetallic main stage vein formation at Butte, Montana (USA): Combining trace element geochemistry and fluid inclusion study in coexisting ore and gangue minerals. Universite de Geneve. Ph.D. thesis.

Ortiz-Benavente, B., Benites, D., Torró, L., Laurent, O., Chelle-Michou, C., Casanova, V., and Fontboté, L., 2022. Indium, germanium, gallium and other trace elements in sphalerite, enargite and colusite from high-sulfidation polymetallic mineralization: preliminary data from the Colquijirca district, central Peru. Proc. 16th SGA Biennial Meeting, March 2022, 1:283-286.

Pring, A., Wade, B., McFadden, A., Lenehan, C.E., Cook, N.J., 2020. Coupled substitutions of minor and trace elements in co-existing sphalerite and wurtzite. Minerals 10 (2), 147. https://doi.org/10.3390/min10020147.

Prinz, W. C., 1967. Geology and ore deposits of the Philipsburg District, Granite County, Montana. U.S. Geol. Surv. Bull. 1237. https://doi.org/10.3133/b1237.

Rose, A.W., 1967. Trace elements in sulfide minerals from the Central District, New Mexico and the Bingham District. Utah. Geochim. Cosmochim. Acta 31, 547–585. https://doi.org/10.1016/0016-7037(67)90034-8.

Rottier, B., Kouzmanov, K., Casanova, V., Wälle, M., Fontboté, L., 2018. Cyclic dilution of magmatic metal-rich hypersaline fluids by magmatic low-salinity fluid: a major process generating the giant epithermal polymetallic deposit of Cerro de Pasco, Peru. Econ. Geol. 113, 825–856. https://doi.org/10.5382/econgeo.2018.4573.

Saleh, M., Lynn, K.G., Jacobsohn, L.G., McCloy, J.S., 2019. Luminescence of undoped commercial ZnS crystals: a critical review and new evidence on the role of impurities using photoluminescence and electrical transient spectroscopy. J. Appl. Phys. 125, 075702. https://doi.org/10.1063/1.5084738.

Shannon, R.D., 1976. Revised effective ionic radii and systematic studies of interatomic distances in halides and chalcogenides. Acta Cryst. A32, 751–767. https://doi.org/10.1107/S0567739476001551.

Šoster, A., Erlandsson, V.B., Velojić, M., Gopon, P., 2023. Ultraviolet-photoluminescence and trace element analyses in Ga-rich sphalerite from the Djebel Gustar Zn-Pb deposit Algeria. Ore Geol. Rev. 157, 105474. https://doi.org/10.1016/j.oregeorev.2023.105474.

Stoiber, R.E., 1940. Minor elements in sphalerite. Econ. Geol. 35, 501–519. https://doi.org/10.2113/gsecongeo.35.4.501.

Tomlinson, D.H., Christiansen, E.H., Keith, J.D., Dorais, M.J., Ganske, R., Fernandez, D., Vetz, N., Sorensen, M., Gibbs, J., 2021. Nature and origin of zoned polymetallic (Pb-Zn-Cu-Ag-Au) veins from the Bingham Canyon porphyry Cu-Au-Mo deposit Utah. Econ. Geol. 116, 747–771. https://doi.org/10.5382/econgeo.4798.

Torró, L., Millán-Nuñez, A.J., Benites, D., González-Jiménez, J.M., Laurent, O., Tavazzani, L., Vallance, J., Chelle-Michou, C., Proenza, J.A., Flores, C., Melgarejo, J. C., 2023. Germanium-and gallium-rich sphalerite in Mississippi Valley–type deposits: the San Vicente district and the Shalipayco deposit Peru. Miner. Deposita 58, 853–880.

Walker, D. D., 1960. Tungsten resources of Montana: Deposits of the Philipsburg Batholith, Granite and Deer Lodge Counties. U.S. Bur. Mines, Report Invest. 5612.

Worthington, J.E., 2007. Porphyry and other molybdenum deposits of Idaho and Montana. Idaho Geol. Surv., Tech. Rept. 07–3, 22p.

Ye, L., Cook, N.J., Ciobanu, C.L., Yuping, L., Qian, Z., Tiegeng, L., Wei, G., Yulong, Y., Danyushevskiy, L., 2011. Trace and minor elements in sphalerite from base metal deposits in south China: a LA-ICPMS study. Ore Geol. Rev. 39 (4), 188–217. https://doi.org/10.1016/j.oregeorev.2011.03.001.